
MEASURING THE PHASE BETWEEN FLUCTUATING PRESSURE AND FLAME RADIATION INTENSITY IN A CYLINDRICAL COMBUSTION CHAMBER

S. Gröning¹, J. S. Hardi¹, D. Suslov¹, and M. Oswald^{1,2}

¹German Aerospace Center (DLR), Institute of Space Propulsion
Im Langen Grund, Hardthausen 74239, Germany

²Institute of Jet Propulsion and Turbomachinery, RWTH Aachen University
55 Templergraben, Aachen 52062, Germany

The energy transfer from the heat release of the combustion to the acoustic pressure oscillations is the driving element of combustion instabilities. This energy transfer is described by the Rayleigh criterion and depends on the phase shift between the pressure and heat release rate oscillations. A research rocket engine combustor, operated with the propellant combination hydrogen/oxygen, was equipped with dynamic pressure sensors and fibre optical probes to measure the flame radiation. This setup has been used for a phase shift analysis study which showed that unstable operation is characterized by a phase shift leading to an energy transfer from the heat release to the acoustic pressure oscillations.

1 INTRODUCTION

High-frequency (HF) combustion instability in liquid propellant rocket engines (LPREs) is a problem which is known since the beginning of the development of these engines [1]. Extensive studies were carried out all over the world starting in the 1950s [2–4]. Due to the complexity of the problem, reliable predictive capabilities could not be developed so far. Experimental research of combustion instabilities aims at understanding the underlying physical processes and mechanisms being responsible for this phenomenon. This fundamental knowledge is required for the development of stability prediction tools [5, 6].

The random pressure oscillations created by the combustion process or by turbulence cause an excitation of the acoustic resonance modes of the combustion chamber. These oscillations can result in oscillatory combustion, causing

a periodic modulation of the heat release rate. Rayleigh postulated in 1878 that an acoustic oscillation is excited if heat is added at the moment of greatest compression or subtracted at the moment of greatest expansion [7,8]. This so called Rayleigh criterion has been formulated in a simple mathematical way by Putnam and Dennis [9,10]:

$$\int_{\text{cycle}} \dot{q}' p' dt > 0. \quad (1)$$

This formulation neglects damping and requires that the time integral over a cycle of the oscillation of the pressure p' and the volumetric heat release rate \dot{q}' must be greater than zero. If monofrequent oscillations are assumed, this means that the absolute value of the phase angle between both oscillations must be between 0 and $\pi/2$. If the Rayleigh criterion is fulfilled, energy is transferred from the heat release to the acoustic oscillations. This causes a rapid increase of the acoustic pressure oscillation amplitudes which can lead to damage or even the destruction of the whole engine, which is then called combustion instability [11]. If the absolute values of the phase angle is between $\pi/2$ and π , the oscillation is damped.

Self-excited combustion instabilities of the first tangential (1T) mode were found in a research hydrogen/oxygen rocket engine combustor named BKD. During unstable operation, the amplitude of the pressure oscillation shows large fluctuations [12]. This is an indication that the Rayleigh criterion according to inequality (1) is not permanently fulfilled, causing a varying energy transfer. The research combustor BKD is equipped with dynamic pressure sensors to measure the acoustic pressure oscillations and fibre optical probes to analyze the oscillation of the combustion process. This setup can be used as an experimental platform in order to analyze the pressure and heat release rate oscillation according to inequality (1).

In the past, phase shift analysis studies were performed especially under forced excitation conditions [13–17]. The used research combustors were equipped with large combustion chamber windows in order to measure the flame radiation intensity with high-speed cameras or photomultiplier (PM) detectors. Richecoeur *et al.* [13] performed a direct comparison between PM signals and dynamic pressure sensor signals from a rectangular chamber under the assumption of a perfectly standing mode. This is possible, although the dynamic pressure sensors are not located at the position, the radiation captured by the PM originates from; as for a standing mode, the phase on one side of the nodal line is position independent. The same approach was used by Knapp and Oswald [14,15] for a cylindrical chamber. Due to the external forcing with a secondary nozzle and a siren wheel, also, here, a standing mode with a fixed position of the nodal line is present. Sliphorst *et al.* [16] used the same cylindrical combustor for the comparison of a two-dimensional intensity field, captured by high-speed

imaging, with a reconstructed pressure field. A standing eigenmode solution was fitted to the dynamic pressure sensor signals, measured on the combustion chamber wall, in order to obtain the pressure information in the camera field of view. The same approach was applied to a rectangular combustion chamber with representative operating conditions and forced acoustics by Hardi *et al.* [17]. Wierman *et al.* [18] performed phase shift studies with research combustors experiencing self-excited combustion instabilities. Proper orthogonal decomposition (POD) techniques were applied to the high-speed imaging of flame radiation intensity. The resulting POD modes are compared to local pressure and velocity fields obtained by means of interpolation methods. Similar work was performed by Quinlan and Zinn [19] using dynamic mode decomposition (DMD) techniques of high-speed imaging from a research combustor experiencing natural instabilities. Bedard *et al.* [20,21] use fibre optical probes instead of a combustion chamber window. Dynamic pressure sensors are placed close to the locations where the flame radiation intensity is measured. This allows a direct comparison between the signals, measured by the fibre optical probes and the dynamic pressure sensors. The probes are connected to a spectrometer in order to observe not only the temporal fluctuation but also the flame emission spectrum. Interpretation of the flame radiation measurements is performed on the basis of an accompanying computational fluid dynamics (CFD) simulation including a detailed chemistry model, similar to the approach of Fiala and Sattelmayer [22].

Most of the described approaches have in common that the pressure and flame radiation intensity, which is used as an approximation for the heat release rate, are not measured at the same location. The flame emission is measured by using combustion chamber windows providing optical access to large portions of the flame. On the other hand, the pressure is measured with sensors on the combustion chamber wall, making it necessary to calculate the phase of the pressure oscillation at the locations of the flame radiation measurement. In the case of standing modes, it is usually assumed that the phase on one side of the nodal line is position independent and, therefore, the same as on the chamber wall. Improved approaches use eigenmode solutions, fitted to the pressure sensor signals, in order to reconstruct the pressure field and obtain a more thorough estimation of the nodal line position. Other approaches simply use interpolation methods. Placing the dynamic pressure sensors in the vicinity of the location, where the captured radiation originates from, is often not possible.

The cylindrical shape and the representative operating conditions of the research combustor BKD, used for the present work, place sharp constraints on the positioning of pressure sensors and optical diagnostics. For this reason, fibre optical probes are used instead of combustion chamber windows. A placement of dynamic pressure sensors in the vicinity of the radiation measurement locations is not possible. Due to its cylindrical shape, the combustor experiences rotat-

ing tangential modes [12, 23] causing a position dependent phase of the pressure oscillations. The methodology to calculate the pressure oscillation at the position, the radiation captured by the fibre optical probes originates from, must be able to account for this effect. A pressure field reconstruction procedure [24] is, therefore, used to process the dynamic pressure sensor signals and to calculate the amplitude and orientation of the 1T mode pressure field. The flame emission of the excited hydroxyl radical (OH^*) [25] is measured for selected injector positions. The results of the pressure field reconstruction procedure are used to calculate the pressure oscillation for the selected positions. As a result, for each position, two signals are obtained which are used for a phase shift analysis study.

Using this methodology, two selected load points, one stable and one unstable, have been analyzed. In both cases, the phase shift is continuously varying and shows a fluctuating behavior on the time scales of a few 1T oscillation periods. Statistical analysis were performed on the obtained phase shift signals in order to identify any structure. For both load points, on large time scales, all phase shift signals show a rather continuous increase or decrease, showing that the pressure and OH^* intensity do not oscillate with the same frequency. The calculation of the probability distribution shows that the phase shift signals for the unstable load point are characterized by a concentration of phase shift values in the region around zero which is in agreement with the Rayleigh criterion. The same analysis for the stable load point shows a different result. Here, only a slight, much less pronounced concentration can be found. This shows significantly different structures in the phase shift signals of a stable and unstable load point.

2 EXPERIMENTAL SETUP

The test specimen used for this investigation is the research combustor BKD [26, 27] with the injector head L42, operated at the P8 test facility [28–30] of the DLR Institute of Space Propulsion in Lampoldshausen. It consists of the injector head, the cylinder segment and the nozzle segment, as shown in Fig. 1a. The L42 injector head has 42 shear coaxial injectors and is operated with the propellant combination hydrogen/oxygen. The combustion chamber has a cylindrical shape with a diameter of 80 mm. The nozzle throat diameter is 50 mm which leads to a contraction ratio of 2.56. The maximum combustion chamber pressure (p_{cc}) during the test run which was used for the presented analysis is 80 bar. The highest mixture ratio ($\text{ROF} = \dot{m}_{\text{O}_2}/\dot{m}_{\text{H}_2}$) is 6.0. For the load point $p_{cc} = 80$ bar with $\text{ROF} = 6.0$, the total propellant mass flow rate is 6.7 kg/s.

According to inequality (1), the evaluation of the Rayleigh criterion requires the simultaneous measurement of the acoustic pressure oscillation $p'(t)$ and the

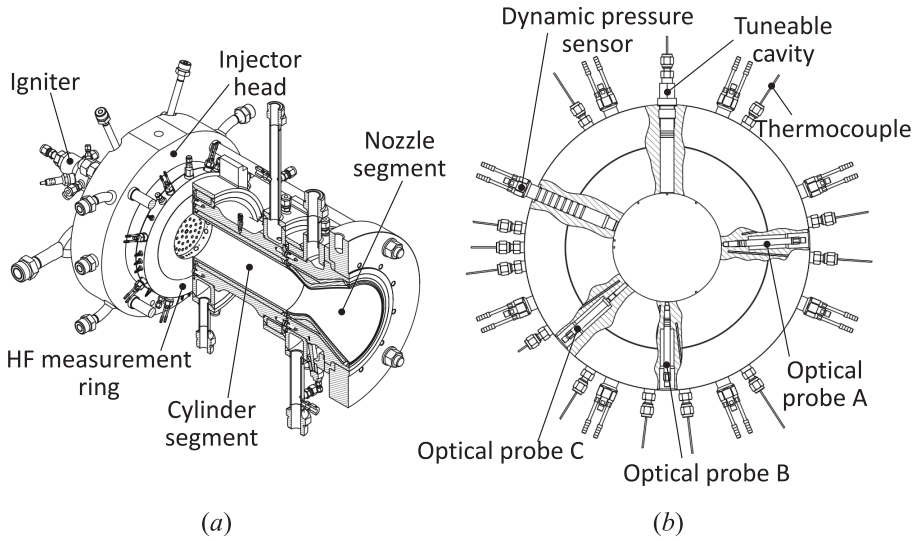


Figure 1 Combustion chamber BKD (a) with HF measurement ring (b)

volumetric heat release rate $\dot{q}'(t)$. The measurement of $p'(t)$ can be achieved relatively easy by the installation of dynamic pressure sensors. The measurement of $\dot{q}'(t)$ is much more challenging, especially at the conditions found in rocket engines [31]. Usually, the measurement of $\dot{q}'(t)$ is approximated using the flame radiation which is easy to measure. In hydrogen/oxygen combustion, the radiation of OH^* [25] has been used as a marker for $\dot{q}'(t)$ due to its good detectability [31, 32]. This is also the approach chosen for the presented work. As discussed in detail in other work by the authors [33], the selected measurement setup allows the measured OH^* radiation intensity signals to be interpreted as an approximation for the oscillation of \dot{q}' [32]. For the described analysis method, only the frequency and phase information of the $\dot{q}'(t)$ signal and not the amplitudes are required. Because the exact relationship between $\dot{q}'(t)$ and the OH^* radiation intensity $I'(t)$ cannot be determined for the used setup, the phase shift between pressure $p'(t)$ and OH^* radiation intensity $I'(t)$ is analyzed instead. Although the exact relationship between $\dot{q}'(t)$ and $I'(t)$ remains undetermined, dominant frequencies in the $I'(t)$ signals and their phase relation characterize the modulation of the combustion process.

In order to measure the $p'(t)$ oscillations in the combustion chamber as well as the fluctuations of the OH^* intensity $I'(t)$, the BKD combustor is equipped with a specially designed HF measurement ring, as shown in Fig. 1b. This ring is installed between the injector head and the cylindrical combustion chamber

segment, as shown in Fig. 1a. It is equipped with 8 flush mounted, water cooled Kistler dynamic pressure sensors with an equiangular spacing of 45° . The dynamic pressure sensor signals $p'_{\text{p dyn}}(t)$ are sampled with a sampling frequency of 100 kHz.

In order to measure the flame radiation at specific locations, the HF measurement ring is equipped with three fibre optical probes. This method of obtaining an optical access to the combustion chamber with minor modifications of the engine is well known in the field of reciprocating engines [34, 35]. Due to higher seal demands when using hydrogen as a fuel, this technology had to be adapted to LPREs with the propellant combination hydrogen/oxygen. A small sapphire rod is installed in the optical probe which creates the optical access. The full acceptance angle of the optical probes is approximately 2° . The radiation captured by the probes is transferred to PM detectors using an optical fibre.

In order to extract the OH^* radiation, the PMs are equipped with interference filters with a center wavelength of 310 nm. Like the $p'_{\text{p dyn}}(t)$ signals, also, the $I'(t)$ signals are sampled with a sampling frequency of 100 kHz.

The narrow field of view of the fibre optical probes is used to align the probes to three specific injectors of the outer ring of the injector pattern as shown in Fig. 2. The selection of the injectors is based on the mode symmetry of the 1T mode. The angular distance between the nodal line and a pressure antinode of the 1T mode is 90° . Probes A and B are, therefore, aligned to the injectors 19 and 13 with an angular distance of 90° . Probe C is aligned to injector 10 with an angular distance of 45° to injector 13. Probe B is aligned to the center of the injector while probes A and C are aligned tangentially to the reaction zone.

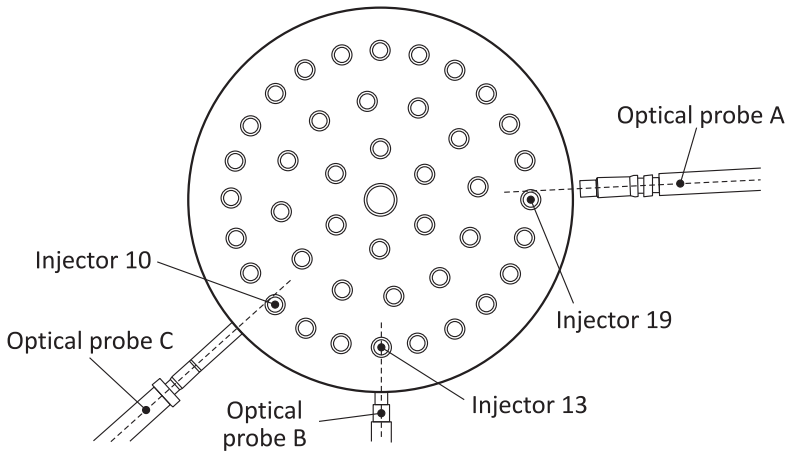


Figure 2 Alignment of fibre optical probes to selected injectors

The alignment of probes A and C has shown to improve the signal quality as a larger part of the reaction zone lies within the field of view. On the other hand, this alignment is more sensitive to capture radiation coming from other injectors.

3 DATA ANALYSIS METHODOLOGY

3.1 Pressure Field Reconstruction

The 1T mode pressure field reconstruction algorithm [24] was originally developed for the CRC (Common Research Chamber) research combustor [36]. The pressure oscillations are measured on the wall of a cylindrical combustion chamber. The amplitude and orientation of the 1T pressure field as functions of time are determined in the measurement plane described by the dynamic pressure sensors. The procedure has been successfully applied to data from the BKD test series [12, 23].

The basis of the pressure field reconstruction algorithm is the fact that the wall pressure distribution of the 1T mode is a sine function with one period in circumferential direction. The first step is to band pass filter the dynamic pressure sensor signals $p'_{\text{pdyn}}(t)$ signals to extract only the contribution of the 1T mode. A two-way filtering procedure [37] in combination with a Butterworth filter of second order is used to avoid a phase shift of the signal during filtering. In the case of the BKD HF measurement ring, for each sample of the $p'_{\text{pdyn}}(t)$ signals, 8 data points consisting of an angular position θ and a pressure value p' are available. A sine function with three parameters (A , φ , and p_{off}) is fitted to this data set:

$$p'(\theta) = A \sin(\theta - \varphi) + p_{\text{off}}. \quad (2)$$

The p_{off} was introduced into the algorithm to account for oscillations with frequencies in the filter band and same phases at all sensor positions [24]. While in the CRC research combustor the values of p_{off} could reach the levels of the amplitude A , in BKD p_{off} is of minor importance but is kept in the algorithm to improve the fit quality. For the data sets used in this work, the average values of p_{off} are 1.3% and 8.8% relative to the envelope of $A(t)$. If the sine function described by Eq. (2) is known, the whole 1T pressure field is known. This step is performed for each sample of the $p'_{\text{pdyn}}(t)$ signals; so, as a result, three signals $A(t)$, $\varphi(t)$, and $p_{\text{off}}(t)$ are obtained.

These three signals completely describe the temporal evolution of the 1T mode pressure field in the measurement plane of the HF measurement ring. They provide the possibility to calculate the $p'(t)$ signal of the 1T mode at any given position in this plane. Here, they are used to calculate the $p'(t)$ signal of the 1T mode at the positions of the three injectors, observed by the fibre optical probes.

Like in the case of the CRC research combustor [24], a complicated rotation behavior of the 1T mode with continuous changes from rotating to standing modes including changes of the rotation direction is observed. As described in [12, 23], the rotation behavior is also affected by the oscillation amplitude. While stable load points show stochastic variations of the rotation mode with nearly no structure, a statistical analysis of the unstable load points indicates a more organized behavior by showing, for example, a preferred orientation of the 1T mode [12].

3.2 Pressure Signal Calculation

Based on the fundamental equations of cylinder acoustics [38], the pressure field of the 1T mode is described by

$$p'(r, \theta, t) = J_1 \left(\frac{\pi \alpha_{01} r}{R} \right) [M \cos(\theta + \omega t - \delta_1) + N \cos(\theta - \omega t - \delta_2)] \quad (3)$$

where r and θ are the polar coordinates; t is the time; J_1 is the Bessel function of the first kind and first order; α_{01} is the first root of the derivative of J_1 [38]; R is the radius of the cylinder; M and N are the amplitude constants; ω is the oscillation frequency of the 1T mode; and δ_1 and δ_2 are the phase constants. To obtain the wall pressure distribution, Eq. (3) is evaluated on the cylinder wall ($r = R$):

$$p'(\theta, t) = J_1(\pi \alpha_{01}) [M \cos(\theta + \omega t - \delta_1) + N \cos(\theta - \omega t - \delta_2)]. \quad (4)$$

Equation (4) can be transformed to a simple sine function with a varying amplitude $A(t)$ and a varying phase $\varphi(t)$ as has been shown previously [24]:

$$p'(\theta, t) = A(t) \sin(\theta - \varphi(t)). \quad (5)$$

The combination of Eqs. (3)–(5) together with the introduction of the $p_{\text{off}}(t)$ signal leads to

$$p'(r, \theta, t) = A(t) \frac{J_1(\pi \alpha_{01} r/R)}{J_1(\pi \alpha_{01})} \sin(\theta - \varphi(t)) + p_{\text{off}}(t). \quad (6)$$

If the radius (r) is set to the radius of the cylinder (R), Eq. (6) reduces to Eq. (2) which is the equation for the wall pressure distribution in the pressure field reconstruction algorithm.

If the signals $A(t)$, $\varphi(t)$, and $p_{\text{off}}(t)$ of the pressure field reconstruction algorithm are used as input for Eq. (6), it can be used to calculate the $p'(t)$ signals of the 1T mode at any given position within the measurement plane of the HF measurement ring ($r \leq R$, $\theta \in [0^\circ, 360^\circ)$).

3.3 Phase Analysis Methodology

The $I'(t)$ signals are filtered with the same filter settings which were used for the filtering of the raw $p'_{\text{pdyn}}(t)$ signals of the dynamic pressure sensors in the pressure field reconstruction procedure. This way the same frequency band is extracted out of the $I'(t)$ signals which was extracted out of the raw $p'_{\text{pdyn}}(t)$ signals. The $p'(t)$ and $I'(t)$ signals now can be compared directly in order to calculate the phase shift signal $\psi(t)$.

The first comparison of the two signals shows that the phase relation between them is not constant but continuously varying. For this reason, the procedure to calculate ψ must be able to handle a varying ψ between the analyzed signals. Different approaches have been investigated in their ability to calculate the $\psi(t)$ signals for the BKD test runs. A general assumption which is common for all approaches is that both signals oscillate with the same frequency and can, therefore, be described by

$$\begin{aligned} p'(t) &= \sin(\omega t - \phi_p(t)) ; \\ I'(t) &= \sin(\omega t - \phi_I(t)) . \end{aligned}$$

It will be later shown that this assumption is not perfectly correct as the oscillation frequencies of $p'(t)$ and $I'(t)$ are not identical. The approach to calculate the $\psi(t)$ signal is still valid as a frequency difference can also be represented by a linearly increasing or decreasing $\psi(t)$.

In order to capture a varying ψ between both signals, common to all investigated approaches is the division of both signals into blocks of time. In each block, ψ is assumed to be constant. By calculating ψ for each block, a varying $\psi(t)$ signal is obtained. The length of the blocks must be adjusted according to the rate of change of ψ . If ψ varies slowly, the block length can be large to reduce the number of blocks and to decrease the computation time. Another advantage is that more data is available per block which facilitates the calculation of ψ . If ψ varies quickly compared to the oscillation frequency of the input signals, the block length must be small. This can be problematic if the block length becomes smaller than the period of one oscillation. Short blocks hinder the calculation of ψ for some approaches. In the case of the BKD data, it was observed that ψ shows quick variations which makes it necessary to use a small block size of less than one oscillation period.

Besides the division of the signals into blocks of time, another step which is common to all investigated procedures is the normalization of the input signals to facilitate the computation of ψ . Due to the band pass filtering, both input signals are nearly monofrequent. This is a requirement for the whole methodology as the oscillation frequency of both signals is assumed to be equal and constant. This nearly monofrequent character of the signals enables an easy way to calculate the amplitude (envelope) signal by determining the maxima and minima of the

signal. The input signal is then divided by the amplitude signal in order to obtain a signal with a constant amplitude of one.

Due to the small block size required for the BKD data, the cross-correlation method which has been used previously to calculate the $\psi(t)$ signal for data of the CRC research combustor [16] was not applicable anymore as it caused large inaccuracies. For the same reason, the determination of ψ by the measurement of the position of the zero crossing which creates very accurate results is not applicable. Therefore, a phase fitting procedure has been used which worked well with small block sizes and showed good accuracy. As the phase of both signals and, therefore, also the phase shift ψ is assumed to be constant in each block, the normalized $p'(t)$ and $I'(t)$ inside the block are represented by

$$p'(t) = \sin(\omega t - \phi_p) ;$$

$$I'(t) = \sin(\omega t - \phi_I) .$$

A sine function with one parameter (ϕ_{fit}) is fitted to both signals inside the block using a least-squares fitting procedure to obtain the values of ϕ_p and ϕ_I :

$$y(t) = \sin(\omega t - \phi_{\text{fit}}) .$$

These values are then used to calculate the phase shift:

$$\psi = \phi_p - \phi_I .$$

The $\psi(t)$ signal with the sampling frequency of the $p'(t)$ and $I'(t)$ signals is then obtained using a cubic spline interpolation with the ψ values of the blocks as input data. An example result of this procedure to calculate the $\psi(t)$ signal is shown in Fig. 3. The plot shows the normalized input signals $p'(t)$ and $I'(t)$ together with the ψ values of the blocks and the interpolated $\psi(t)$ signal.

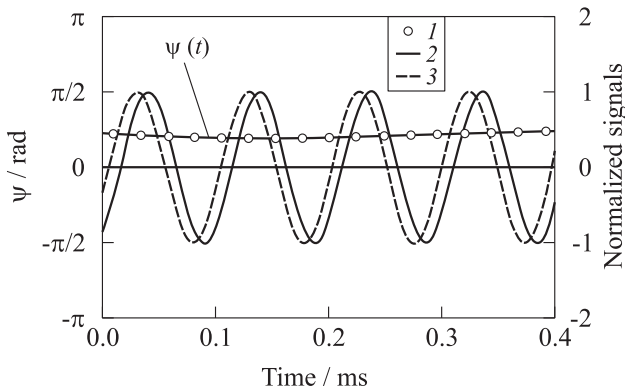


Figure 3 Example result of the phase fitting procedure: 1 — ψ values of the blocks; 2 — normalized $p'(t)$; and 3 — normalized $I'(t)$

3.4 Validation of Methodology

The methodology to calculate the $\psi(t)$ signal presented here is a chain of different subprocedures. It consists of a number of substeps to get from the raw data of the $p'_{\text{p dyn}}(t)$ signals and the $I'(t)$ signals to the final result of the $\psi(t)$ signal. Therefore, each substep of the methodology has been tested and validated before the whole procedure was applied to the BKD test data.

The pressure field reconstruction algorithm has been used several times for data from the CRC research combustor [24] and the BKD [12,23]. It is, therefore, seen as tested and validated at this point. In the work presented here, it is tested together with the procedure from subsection 3.2 as a single module in order to validate Eq. (6). The second subprocedure which requires testing and validation is the procedure to calculate the $\psi(t)$ signal described in subsection 3.3.

To test the pressure field reconstruction together with the methodology from subsection 3.2, a 1T pressure field was simulated using Eq. (3). This equation has been used to calculate the signals $p'_{\text{p dyn}}(t)$ of 8 dynamic pressure sensors. Furthermore, this equation was used to calculate the $p'(t)$ signal at a selected test position. Here, for this test position, the position of injector 10 has been chosen. The simulated sensor signals $p'_{\text{p dyn}}(t)$ were then used as input for the pressure field reconstruction algorithm and the signals $A(t)$, $\varphi(t)$, and $p_{\text{off}}(t)$ were obtained. These signals were then used as input for Eq. (6) to calculate the $p'(t)$ signal at the test position. Then, this signal was compared with the signal at the test position which was calculated using Eq. (3) together with the simulated $p'_{\text{p dyn}}(t)$ signals. The result is shown in Fig. 4a. The good agreement between the simulated $p'(t)$ signal and the signal obtained with Eq. (6) shows the proper functioning of the procedure.

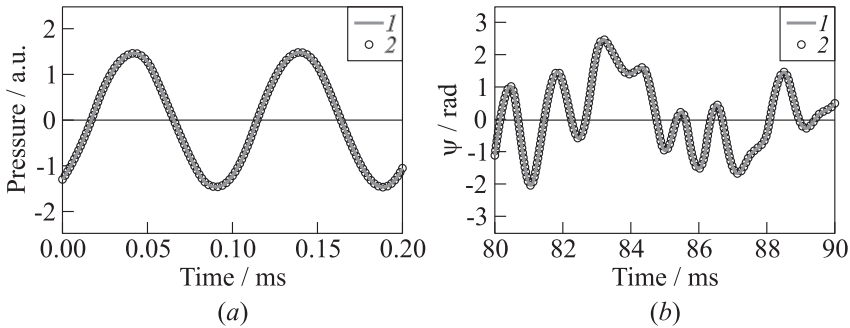


Figure 4 Validation of methodology: (a) signal at the test position calculated using the pressure field reconstruction; (b) reconstruction of a simulated $\psi(t)$ signal; 1 — simulated signal; and 2 — reconstructed signal

The phase shift calculation procedure from subsection 3.3 is validated by simulating two signals $y_1(t)$ and $y_2(t)$ with a known $\psi(t)$ signal and by testing the ability of the procedure to reconstruct this $\psi(t)$ signal:

$$\begin{aligned} y_1(t) &= A_1(t) \sin(\omega t) ; \\ y_2(t) &= A_2(t) \sin(\omega t - \phi(t)) . \end{aligned} \quad (7)$$

The amplitude signals $A_1(t)$ and $A_2(t)$ as well as the phase shift signal $\psi(t)$ were simulated using a random number generator. The signals $y_1(t)$ and $y_2(t)$ were then used as input for the phase shift calculation procedure. As a result of this procedure, the phase shift signal $\psi(t)$ is obtained which is then compared with the simulated signal used in Eq. (7). The result is shown in Fig. 4b. The good agreement between the simulated and the reconstructed $\psi(t)$ signal shows the proper functioning of the methodology described in subsection 3.3.

4 APPLICATION TO TEST DATA

The presented analysis methodology was applied to two selected load points of a single test run of the BKD test series. These load points were selected as they incorporate one stable and one unstable load points. Figure 5 shows the test sequence of the selected test run with the signals of the combustion chamber pressure $p_{cc}(t)$ and mixture ratio $ROF(t)$ together with one $p'_{p_{dyn}}(t)$ signal of the dynamic pressure sensors in the HF measurement ring. The $p'_{p_{dyn}}(t)$ signal shows increased oscillation amplitudes for the load point $p_{cc} = 80$ bar, $ROF = 6$. This is an instability of the 1T mode as was shown in [12,23]. For the phase shift analysis, this unstable load point (LP3) together with a stable load point (LP7, $p_{cc} = 60$ bar, $ROF = 4$) were selected. The corresponding analysis windows with a length of 1 s are marked in Fig. 5 with grey areas.

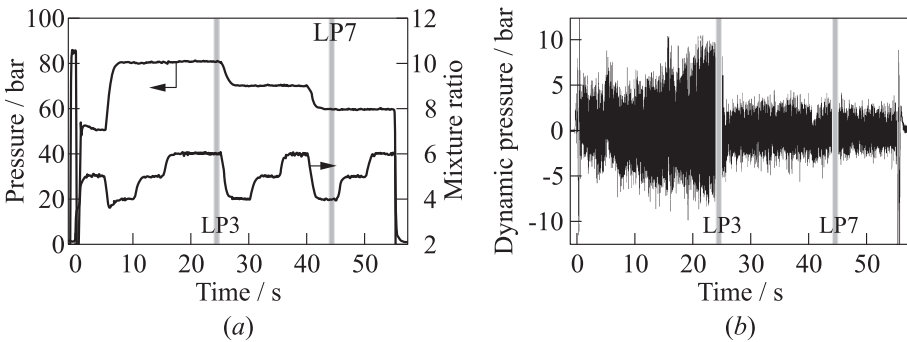


Figure 5 Test sequence of the selected test run with definition of analysis windows: (a) test sequence; and (b) dynamic pressure sensor signal

For each analysis window, eight $p'_{\text{p dyn}}(t)$ and three $I'(t)$ signals are available. For the selected analysis windows, the $\psi(t)$ signals were calculated for the three injector positions observed by the fibre optical probes. Therefore, a total number of six $\psi(t)$ signals were calculated, three for LP3 and three for LP7.

Table 1 Injector coordinates

Injector	r , mm	θ	Probe
10	31	225°	C
13	31	270°	B
19	31	0°	A

The band pass filter for the pressure field reconstruction algorithm is centered to the 1T frequency of the corresponding load point. For LP3, this is $f_{\text{LP3}} = 10\,239$ Hz, and for LP7, $f_{\text{LP7}} = 10\,605$ Hz. The pass band width was set to 2800 Hz. In order to better resolve the rotational character of the 1T mode, the signals are upsampled to a sampling frequency of 800 kHz [12, 23, 24]. Using the results of the pressure field reconstruction, the $p'(t)$ signals of the 1T mode are calculated for the three injector positions using the coordinates shown in Table 1. The $I'(t)$ signals were filtered with the same settings as the $p'_{\text{p dyn}}(t)$ signals. The $\psi(t)$ signal is calculated with a block length of 0.5 periods of the 1T frequency with an overlap of 0.25 periods.

5 RESULTS

Figure 6 shows an example $\psi(t)$ signal as a result of the phase shift calculation. The example is taken from the analysis of the unstable load point LP3. The plot shows the normalized $p'(t)$ signal at the position of injector 10 together with the normalized $I'(t)$ signal of probe C and the calculated $\psi(t)$ signal. A length of 5 ms which is 0.5% of the full length of the analysis window is plotted. The $\psi(t)$ signal has been limited to the interval $[-\pi, \pi]$. Figure 6 clearly shows that the $\psi(t)$ signal is characterized by a fluctuating behavior on the time scales of a few 1T oscillation periods which is the case for all 6 calculated $\psi(t)$ signals. Therefore, statistical approaches are required in order to analyze the $\psi(t)$ signals.

Generally, there are two ways to represent the $\psi(t)$ signal. First, the signal can be limited to the interval $[-\pi, \pi]$ as has been done for the plot in Fig. 6. This representation is required to analyze the signal with regard to the Rayleigh criterion. Second, the values of $\psi(t)$ can be represented without any limitation to a specific interval. This enables to analyze the signals in a different way: if both oscillations, $p'(t)$ and $I'(t)$, are characterized by slightly different oscillation frequencies, this causes a continuous increase or decrease of the $\psi(t)$ signal.

Figure 7 shows the plot of all 6 calculated $\psi(t)$ signals with no limitation to the interval $[-\pi, \pi]$. In Fig. 7a, the signals of the three injectors are plotted for

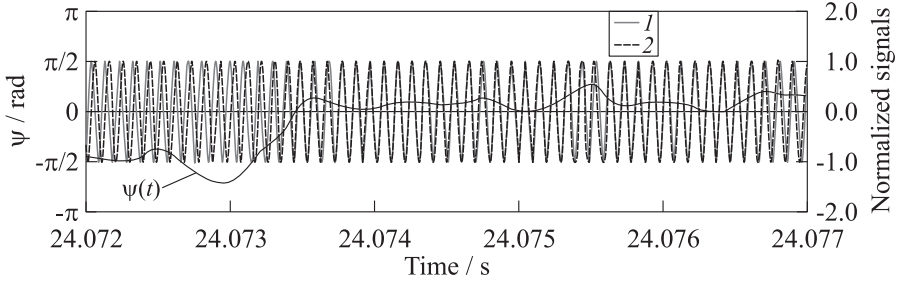


Figure 6 Example result of the phase shift calculation: 1 — normalized $p'(t)$; and 2 — normalized $I'(t)$

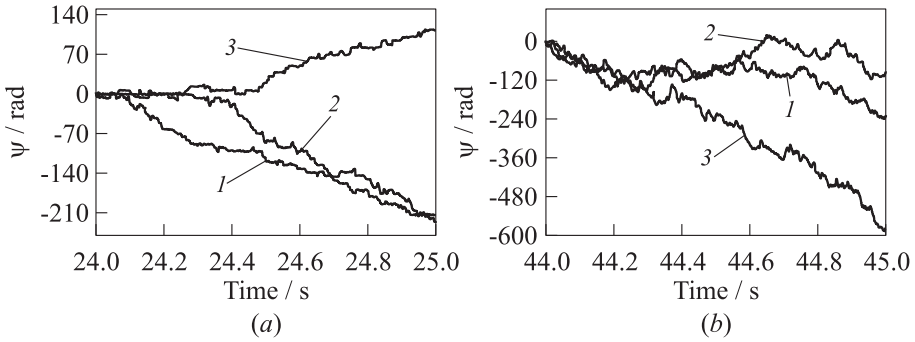


Figure 7 Plot of the 6 phase shift signals with no limitation to the interval $[-\pi, \pi]$: (a) unstable load point LP3; (b) stable load point LP7; 1 — injector 10; 2 — injector 13; and 3 — injector 19

the unstable load point and in Fig. 7b, for the stable load point. For both load points, an average increase or decrease of the $\psi(t)$ signals is observed, showing that the average oscillation frequencies of $p'(t)$ and $I'(t)$ are indeed not identical. Furthermore, for both load points, the behavior of all three signals is different. For LP3, injectors 10 and 13 show a general decrease while injector 19 shows a general increase. For LP7, injector 19 shows a stronger general decrease than injectors 10 and 13. An interesting aspect is that in both cases, injector 19 shows a significantly different behavior than the other two injectors. The plots show further a difference between the stable and unstable load point. For LP3, all $\psi(t)$ signals are characterized by a stepwise character. The signals stay in a specific region and then show a sudden jump. The signals of LP7 show a more continuous variation.

For both cases, the increase or decrease of the $\psi(t)$ signals on long time scales shows that the frequencies of $p'(t)$ and $I'(t)$ are not identical. The fre-

Table 2 Average frequency differences estimated from Fig. 7

Injector	LP3		LP7	
	$\Delta\omega$, 1/s	Δf , Hz	$\Delta\omega$, 1/s	Δf , Hz
10	-220	-35	-220	-35
13	-220	-35	-100	-16
19	120	19	-600	-95

quency of the $p'(t)$ signals for the three different positions, on the other hand, is always identical as these signals are created by the 1T mode which has at all positions the same frequency. The fact that the $\psi(t)$ signals for the three different injectors show a different behavior indicates that the three injectors behave differently. In other work by the present authors [33], it was shown that the $I'(t)$ oscillations are created by the injectors. Furthermore, indications were found that the oscillations created by the injectors are rather independent to the oscillations of the chamber pressure. The fact that all injectors create $I'(t)$ oscillations with a slightly different behavior supports these indications.

From the phase shift signals shown in Fig. 7, an average frequency difference between the $p'(t)$ and $I'(t)$ signals can be estimated. These values are summarized in Table 2. The way the $\psi(t)$ signal was calculated, a negative frequency difference Δf means that the average oscillation frequency of $I'(t)$ is lower than the average oscillation frequency of $p'(t)$ and the other way round.

Figure 8 shows the power spectral density (PSD) of the three $I'(t)$ signals for both load points. The peaks of the PSD signals are the injector resonance frequencies [33]. The pass band of the filter has been marked with a grey box.

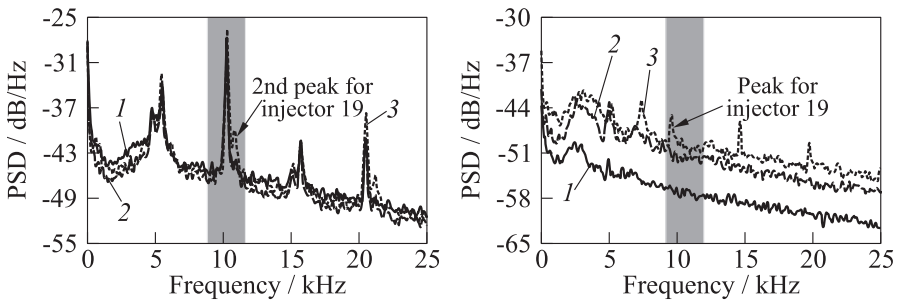


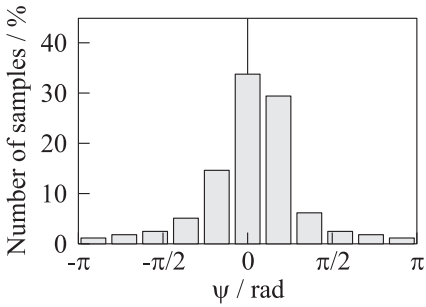
Figure 8 Power spectral density of the PM signals for unstable load point LP3 (a) and stable load point LP7 (b) with filter pass band (grey box): 1 — injector 10; 2 — injector 13; and 3 — injector 19

The PSD signals of the unstable load point show that the $I'(t)$ signal of injector 19 has a second, smaller peak at higher frequencies which the other signals do not have. This means that the $I'(t)$ signal of injector 19 has components at higher frequencies with higher amplitudes compared to the $I'(t)$ signals of the other injectors which is in agreement with Table 2. The PSD signals of the stable load point show that also here, the PSD of the $I'(t)$ signal of injector 19 shows a unique feature compared to the other signals. It shows a peak at approximately 9.5 kHz which does not exist in the PSD data of the other signals. This explains why the $\psi(t)$ signal of injector 19 shows a much clearer trend for the stable load point than the $\psi(t)$ signals of injectors 10 and 13. The PSD data of the $I'(t)$ signals support the results of the phase shift analysis. Furthermore, the phase shift analysis has shown to be a very sensitive analysis methodology which is able to detect features in the signals which would not have been detected with a PSD analysis alone.

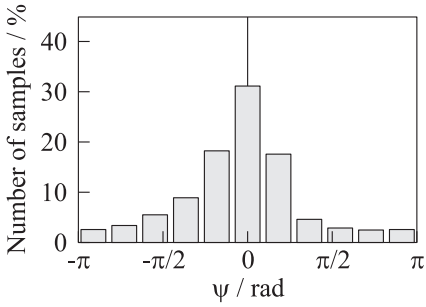
The second analysis which has been applied to the $\psi(t)$ signals is the determination of their probability distribution and representation in the form of a histogram plot. For this analysis, the $\psi(t)$ signals are restricted to the interval $[-\pi, \pi]$. This interval is divided into a number of subintervals. For each sample of the $\psi(t)$ signals, it is decided to which interval it belongs to and the total number of samples of each interval is counted. This is an easy way to determine if there are any intervals in which the signal is to find with a higher probability and to identify if there is any structure in the signal.

Figure 9 shows the histograms of the three $\psi(t)$ signals of the unstable load point LP3. The plots show clearly that all three $\psi(t)$ signals have a strong concentration of samples in the interval around $\psi = 0$. This is generally in agreement with the expectations from the Rayleigh criterion. Around zero, ψ causes an energy transfer from the heat release to the acoustic pressure oscillations. This explains the increased oscillation amplitudes for this load point. Also here, injector 19 shows a slightly different behavior compared to the injectors 10 and 13: the peak of the histogram is shifted slightly to positive values. The strong concentration of samples in a specific interval is in agreement with the results from Fig. 7 where the $\psi(t)$ signals of the unstable load point showed longer periods where they stayed in specific intervals.

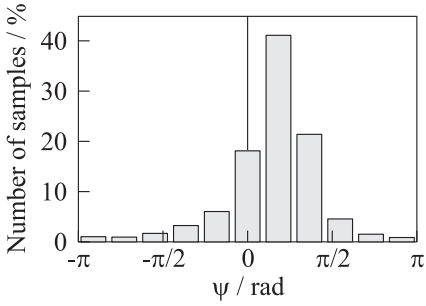
Figure 10 shows the histograms of the three $\psi(t)$ signals of the stable load point LP7. Here, the plots show a completely different structure of the $\psi(t)$ signals compared to the unstable load point. Also here, a slight concentration of samples in specific intervals can be observed but this concentration is much less pronounced compared to the unstable case. Furthermore, this concentration is found in the interval between 0.2π and 0.6π which would result in lower amplification or even damping of the acoustic oscillations according to the Rayleigh criterion. The generally much less pronounced concentration of samples in specific intervals is in agreement with the results from Fig. 7 which shows a much more continuous variation of the $\psi(t)$ signals.



(a)

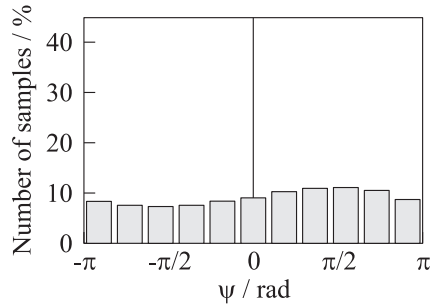


(b)

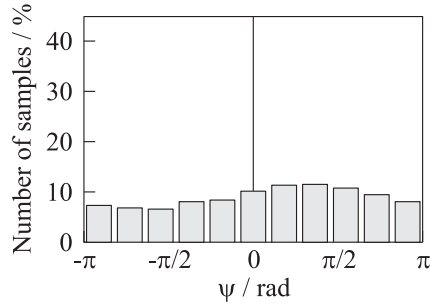


(c)

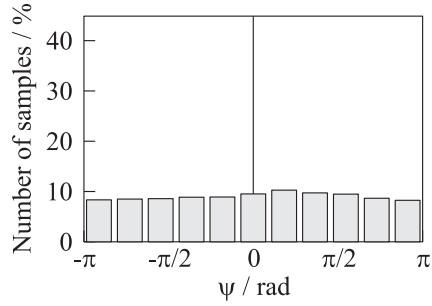
Figure 9 Histograms of the three $\psi(t)$ signals of the unstable load point LP3: (a) injector 10; (b) injector 13; and (c) injector 19



(a)



(b)



(c)

Figure 10 Histograms of the three $\psi(t)$ signals of the stable load point LP7: (a) injector 10; (b) injector 13; and (c) injector 19

It was found that the $\psi(t)$ signals of the stable and unstable load points show significant differences. The signals of the unstable load point show a concentration of samples in a region which causes an amplification of the acoustic pressure oscillations according to the Rayleigh criterion. The signals of the stable load point show a much less pronounced concentration of samples in specific intervals.

This means that periods of damping and driving are more equally distributed for the stable load point while the unstable load point is characterized by longer periods of driving.

6 SUMMARY AND CONCLUDING REMARKS

A phase shift analysis study has been performed with experimental data from a research combustor named BKD. This combustor shows self-excited combustion instabilities of the 1T mode for specific load points. The combustion chamber is equipped with dynamic pressure sensors to measure the acoustic pressure oscillations as well as fibre optical probes to measure the OH* intensity oscillations as an approximation for the heat release rate oscillations. The fibre optical probes are aligned to three selected injectors in order to measure the OH* intensity fluctuation, generated by these injectors. The dynamic pressure sensor signals and the optical signals were processed using a newly developed analysis methodology. This method is able to compare the pressure and intensity signals, although they are measured at different locations with the phase of the pressure oscillations being position dependent due to rotating 1T mode pressure fields.

The dynamic pressure sensor signals are processed with a 1T mode pressure field reconstruction procedure. The results of this procedure are used to calculate the pressure oscillations of the 1T mode at the positions of the three selected injectors. The optical signals are band pass filtered to the frequency of the 1T mode pressure oscillations. As a result of this preparation for all three injector positions, a pressure oscillation and an OH* intensity oscillation signal is available which are used as input for a phase shift analysis procedure. This procedure calculates a phase shift signal which describes the phase shift between the pressure and OH* intensity oscillation.

The analysis methodology has been applied to two selected load points (one stable and one unstable) of a single test run of the BKD test series. Generally, the calculated phase shift signals show that the phase relation between the pressure and OH* intensity oscillation is not constant. The phase shift signals show fluctuations on the time scales of the oscillation frequency of the analyzed signals. On long time scales, on the other hand, they show a trend which can be explained by different oscillation frequencies of the pressure and OH* intensity signals. It has been shown previously that the oscillation frequencies of pressure and OH* are not identical which is supported by the results of the phase shift analysis. Furthermore, the analysis was able to detect differences in the dynamics of the observed injectors. Two injectors show a similar behavior while the third one deviates from the others. The reason for this behavior could not be identified so far but a PSD analysis of the OH* intensity signals supports the results of

the phase shift analysis. The phase shift signals of the unstable load point show a concentration of samples around the value of zero which is in agreement with the Rayleigh criterion. The signals of the stable load point, on the other hand, show a much more equal distribution over the interval $[-\pi, \pi]$, meaning that periods with damping and driving are much more equally distributed for this load point.

The newly developed methodology has shown to be applicable to the experimental data of the BKD test series. It has shown to be able to discover new information about the dynamic processes of BKD. The procedure is a very sensitive analysis method which is able to detect aspects of the dynamic processes with a high level of detail. The complexity of the resulting phase shift signals, on the other hand, hinder the analysis of these signals. Further analysis of the currently calculated 6 signals is, therefore, required. Up to now, the methodology has only been applied to two load points of a single test run. The analysis needs to be extended to other load points and test runs of the BKD test series in order to form a statistical basis for the discovery of general trends which is not possible with the analysis of only two selected load points.

ACKNOWLEDGMENTS

Research undertaken for this paper has been assisted with financial support from the DFG (German Research Foundation) in the framework of the SFB-TR 40. The Authors are grateful to the crew of the P8 test bench as well as Philipp Groß and Mike Ziemßen for their efforts in performing the test runs on which the results presented here are based. Furthermore, the efforts of Joachim Sender concerning the design of the BKD combustor are gratefully acknowledged.

REFERENCES

1. Ross, C. C., and P. P. Datner. 1954. Combustion instability in liquid-propellant rocket motors — a survey. *Selected combustion problems: Fundamentals and aeronautical applications*. Eds. W. R. Hawthorne, J. Fabri, and D. B. Spalding. Butterworths Scientific Publications. Advisory Group for Aeronautical Research and Development North Atlantic Treaty Organization. 352–380.
2. Harrje, D. T., and F. H. Reardon. 1972. Liquid propellant rocket combustion instability. NASA Special Publication No. SP-194.
3. Anderson, W. E., H. M. Ryan, and R. J. Santoro 1991. Combustion instability phenomena of importance to liquid bi-propellant rocket engine. *28th JANNAF Combustion Subcommittee Meeting*. Ed. M. T. Gannaway. Columbia, MD: Chemical Propulsion Information Agency. 99–112.

4. Yang, V., and W.E. Anderson, eds. 1995. *Liquid rocket engine combustion instability*. Progress in astronautics and aeronautics ser. Washington, DC: American Institute of Aeronautics and Astronautics. Vol. 169. 577 p.
5. Pieringer, J., and T. Sattelmayer. 2009. Simulation of combustion instabilities in liquid rocket engines with acoustic perturbation equations. *J. Propul. Power* 25(5):1020–1031.
6. Schulze, M., M. Schmid, D. Morgenweck, S. Köglmeier, and T. Sattelmayer. 2013. A conceptual approach for the prediction of thermoacoustic stability in rocket engines. AIAA Paper No. 2013-3779.
7. Rayleigh, J. W. S. 1878. The explanation of certain acoustical phenomena. *Nature* 18(455):319–321.
8. Rayleigh, J. W. S. 1945. *The theory of sound*. 2nd ed. New York, NY: Dover Publications. Vol. 2. 504 p.
9. Putnam, A. A., and W.R. Dennis. 1953. Organ-pipe oscillations in a flame-filled tube. *4th Symposium (International) on Combustion*. Baltimore, MD: The Williams & Wilkins Co. 566–575.
10. Putnam, A. A., and W. R. Dennis. 1954. Burner oscillations of the gauze-tone type. *J. Acoust. Soc. Am.* 26(5):716–725.
11. Sutton, G. P., and O. Biblarz. 2001. *Rocket propulsion elements*. 7th ed. New York, NY: John Wiley & Sons. 764 p.
12. Gröning, S., M. Oswald, and T. Sattelmayer. 2012. Selbst erregte tangentielle Moden in einer Raketenbrennkammer unter repräsentativen Bedingungen. *61. Deutscher Luft- und Raumfahrtkongress*. Berlin: Deutsche Gesellschaft für Luft- und Raumfahrt — Lilienthal-Oberth e.V.
13. Richecoeur, F., P. Scoufflaire, S. Ducruix, and S. Candel. 2006. High-frequency transverse acoustic coupling in a multiple-injector cryogenic combustor. *J. Propul. Power* 22(4):790–799.
14. Knapp, B., and M. Oswald. 2006. High speed visualization of flame response in a LOx/H₂ combustion chamber during external excitation. *12th Symposium (International) on Flow Visualization*. Göttingen.
15. Oswald, M., and B. Knapp. 2009. Investigation of combustion chamber acoustics and its interaction with LOx/H₂ spray flames. *Progress in propulsion physics*. Eds. L. T. DeLuca, C. Bonnal, O. Haidn, and S. M. Frolov. EUCASS advances in aerospace sciences book ser. 1:205–224.
16. Sliphorst, M., B. Knapp, S. Groening, and M. Oswald. 2012. Combustion instability-coupling mechanisms between liquid oxygen/methane spray flames and acoustics. *J. Propul. Power* 28(6):1339–1350.
17. Hardi, J. S., S. K. Beinke, M. Oswald, and B. B. Dally. 2014. Coupling of cryogenic oxygen–hydrogen flames to longitudinal and transverse acoustic instabilities. *J. Propul. Power* 30(4):991–1004.
18. Wierman, M., B. Pomeroy, T. Feldman, W. Hallum, and W. Anderson. 2012. Application of proper orthogonal decomposition to light intensity measurements of combustion instability. AIAA Paper No. 2012-4203.
19. Quinlan, J. M., and B. T. Zinn. 2014. Transverse combustion instabilities: Modern experimental techniques and analysis. *50th AIAA/ASME/SAE/ASEE Joint*

- Propulsion Conference*. Cleveland, OH: American Institute of Aeronautics and Astronautics.
20. Bedard, M. J., V. S. Sardeshmukh, T. L. Fuller, W. E. Anderson, and M. Tanabe. 2014. Chemiluminescence as a diagnostic in studying combustion instability in a practical combustor. AIAA Paper No. 2014-3660.
 21. Bedard, M. J., V. S. Sardeshmukh, T. L. Fuller, and W. E. Anderson. 2015. Comparison between predicted and measured chemiluminescence in an unstable rocket combustor. *6th European Conference for Aeronautics and Space Sciences*. Krakow.
 22. Fiala, T., and T. Sattelmayer. 2016. Assessment of existing and new modeling strategies for the simulation of OH* radiation in high-temperature flames. *CEAS Space J.* 8(1):47–58.
 23. Gröning, S., D. Suslov, M. Oswald, and T. Sattelmayer. 2013. Stability behaviour of a cylindrical rocket engine combustion chamber operated with liquid hydrogen and liquid oxygen. *5th European Conference for Aeronautics and Space Sciences*. Munich.
 24. Sliphorst, M., S. Gröning, and M. Oswald. 2011. Theoretical and experimental identification of acoustic spinning mode in a cylindrical combustor. *J. Propul. Power* 27(1):182–189.
 25. Gaydon, A. G. 1974. *The spectroscopy of flames*. 2nd ed. London: Chapman and Hall. 424 p.
 26. Suslov, D., A. Woschnak, J. Sender, and M. Oswald. 2003. Test specimen design and measurement technique for investigation of heat transfer processes in cooling channels of rocket engines under real thermal conditions. AIAA Paper No. 2003-4613.
 27. Sender, J., D. I. Suslov, J. Deeken, S. Gröning, and M. Oswald. 2016. “L42” technology demonstrator: Operational experience. *Space Propulsion 2016*. Rome: Association aéronautique et astronautique de France (3AF).
 28. Fröhlke, K., A. Habertzettl, O. J. Haidn, S. Heinrich, M. Sion, and P. Vuillermoz. 1997. First hot fire test campaign at the French/German research facility P8. *33rd AIAA/ASME/SAE/ASEE Joint Propulsion Conference*. Seattle, WA.
 29. Koschel, W., and O. J. Haidn. 1998. P8 — the new French/German test facility for H₂/O₂ high pressure rocket engine combustion research. *Int. J. Hydrogen Energ.* 23(8):683–694.
 30. Habertzettl, A. 2000. European research and technology test bench P8 for high pressure liquid rocket propellants. AIAA Paper No. 2000-3307.
 31. Fiala, T., and T. Sattelmayer. 2013. Heat release and OH*-radiation in laminar non-premixed hydrogen–oxygen flames. *51st AIAA Aerospace Sciences Meeting including the New Horizons Forum and Aerospace Exposition*. Grapevine, TX: American Institute of Aeronautics and Astronautics.
 32. Fiala, T., and T. Sattelmayer. 2013. On the use of OH* radiation as a marker for the heat release rate in high-pressure hydrogen–oxygen liquid rocket combustion. AIAA Paper No. 2013-3780.
 33. Gröning, S., J. S. Hardi, D. Suslov, and M. Oswald. 2016. Injector-driven combustion instabilities in a hydrogen/oxygen rocket combustor. *J. Propul. Power* 32(3):560–573. doi: 10.2514/1.B35768.

34. Spicher, U., and A. Velji. 1985. Measurements of spatial flame propagation and flow velocities in a spark ignition engine. *12th Symposium (International) on Combustion*. 20:19–27.
35. Pöschl, M. 2006. Einfluss von Temperaturinhomogenitäten auf den Reaktionsablauf bei der klopfenden Verbrennung. München: Technische Universität München. Ph.D. Thesis.
36. Knapp, B., Z. Farago, and M. Oswald. 2007. Interaction of LO_x/GH₂ spray-combustion with acoustics. AIAA Paper No. 2007-0572.
37. Stearns, S.D. 1975. *Digital signal analysis*. Rochelle Park, NJ: Hayden Book Co. 280 p.
38. Zucrow, M.J., and J.D. Hoffmann. 1985. *Gas dynamics. Vol. II: Multidimensional flow*. 2nd ed. Malabar, FL: Robert E. Krieger Publishing Co. 487 p.